Pyrolysis of Highly Metallized Polymers: Ceramic Thin Films Containing Magnetic CoFe Alloy Nanoparticles from a Polyferrocenylsilane with Pendant Cobalt Clusters

Kun Liu,[†] Scott B. Clendenning,[†,‡] Lars Friebe,[†] Wing Yan Chan,[†] Xiaobin Zhu,[§,Δ]
Mark R. Freeman,[§] Guo Cheng Yang,[||] Christopher M. Yip,[||] Dan Grozea,[⊥]
Zheng-Hong Lu,[⊥] and Ian Manners*,[†,#]

*Department of Chemistry, University of Toronto, 80 St. George Street, Toronto, Ontario M5S 3H6,
Canada, The School of Chemistry, University of Bristol, Bristol BS8 1TS, United Kingdom, Department of
Physics, University of Alberta, Edmonton, Alberta T6G 2J1, Canada, Department of Chemical Engineering
& Applied Chemistry, Institute Biomaterials & Biochemical Engineering, University of Toronto, Toronto,
Ontario M5S 3G9, Canada, and Department of Materials Science and Engineering, University of Toronto,
Toronto, Ontario M5S 3E4, Canada*

We describe the pyrolysis of a highly metallized polymer precursor comprised of a polyferrocenylsilane with pendant cobalt clusters under a reductive atmosphere ($N_2/H_2 = 92\%/8\%$) leading to CoFe magnetic alloy nanoparticle-containing ceramic thin films. Variation of the pyrolysis conditions leads to changes in the nanoparticle size, size distribution, and composition, as well as the ceramic film structure, all of which influence the magnetic properties of the material. When pyrolyzed at 500 °C, the nucleation and growth afford uniform size, larger CoFe nanoparticles on the film surface, and smaller nanoparticles in the underlying layer of the ceramic films. We found that the SiC/C ceramic matrix prevents oxidation of fully embedded nanoparticles, whereas the surface nanoparticles are oxidized on exposure to air. The nanoparticle-containing films are superparamagnetic when pyrolyzed at 600 °C and are ferromagnetic at higher pyrolysis temperatures. The CoFe nanoparticle-containing ceramic thin films have been characterized by a variety of techniques, which include scanning electron microscopy, transmission electron microscopy, atomic force microscopy, energy-dispersive X-ray analysis, selected-area electron diffraction, X-ray photoelectron spectroscopy, and the magneto-optical Kerr effect.

Introduction

Over the past decade, research activity in the field of metal nanoparticles (NPs) has grown dramatically.[1−3] These efforts are driven by the unique properties of NPs, especially their high surface area-to-volume ratio and quantum size effects. They have found applications as magnetic materials for data storage and in spintronic devices, electrochromic materials, biosensors, and catalysis.[4,5] Metal NPs can be prepared by reducing metal salts in micelles[6] or thin films,[7] by sol processes involving the thermal decomposition of organometallic molecular precursors,[8] and by hydrothermal synthesis.[9] Soluble and readily processable metal-containing polymers are also promising precursors for the synthesis of metal NPs via thermal or radiation treatment. This method is potentially attractive as a wide range of metallopolymers are now available as a result of synthetic developments in the past 10−15 years.[10,11]

As ferrocene and its derivatives are readily available at relatively low cost, ferrocene-based metallopolymers have been recognized as excellent precursors to Fe NPs. For example, in the 1970s Yajima and Omori reported the pyrolysis of a polyacetylferrocene-based resin to yield a glassy matrix containing Fe particles.[12] In addition, Houser

* To whom correspondence should be addressed. E-mail: Ian.Manners@Bristol.ac.uk.
† Department of Chemistry, University of Toronto.
‡ Current address: Intel Corporation, RA3-252, 2513 NW 229th Avenue, Hillsboro, OR 97124.
§ University of Alberta.
|| Department of Chemical Engineering & Applied Chemistry, University of Toronto.
⊥ Department of Materials Science and Engineering, University of Toronto.
University of Bristol.
Δ Current address: Seagate Research Center, 1251 Waterfront Place, Pittsburgh, PA 15222.

(1) Burda, C.; Chen, X. B.; Narayanan, R.; El-Sayed, M. A. *Chem. Rev.* **2005**, *105*, 1025.
(2) (a) Masala, O.; Seshadri, R. *Annu. Rev. Mater. Res.* **2004**, *34*, 41. (b) Leslie-Pelecky, D. L.; Rieke, R. D. *Chem. Mater.* **1996**, *8*, 1770.
(3) Feldheim, D. L.; Foss, C. A., Jr. *Metal Nanoparticles: Synthesis, Characterization, and Applications*; Dekker: New York, 2002.
(4) (a) Herron, N.; Thorn, D. L. *Adv. Mater.* **1998**, *10*, 1173. (b) Desvaux, C.; Amiens, C.; Fejes, P.; Renaud, P.; Respaud, M.; Lecante, P.; Snoeck, E.; Chaudret, B. *Nat. Mater.* **2005**, *4*, 750.
(5) Cahen, D.; Hodes, G. *Adv. Mater.* **2002**, *14*, 789.
(6) Lisiecki, I.; Pileni, M. P. *J. Am. Chem. Soc.* **1993**, *115*, 3887.
(7) Yin, D. H.; Horiuchi, S.; Morita, M.; Takahara, A. *Langmuir* **2005**, *21*, 9352.
(8) Murray, C. B.; Kagan, C. R.; Bawendi, M. G. *Annu. Rev. Mater. Sci.* **2000**, *30*, 545.
(9) Sun, Y.-P.; Rollins, H. W.; Guduru, R. *Chem. Mater.* **1999**, *11*, 7.
(10) (a) Archer, R. D. *Inorganic and Organometallic Polymers*; John Wiley & Sons, Inc.: New York, 2001. (b) Abd-El-Aziz, A. S. *Macromol. Rapid Commun.* **2002**, *23*, 995. (c) Newkome, G. R.; He, E.; Moorefield, C. N. *Chem. Rev.* **1999**, *99*, 1689. (d) Astruc, D.; Chardac, F. *Chem. Rev.* **2001**, *101*, 2991.
(11) (a) Manners, I. *Synthetic Metal-Containing Polymers*; Wiley-VCH: Weinheim, Germany, 2004. (b) Nguyen, P.; Gómez-Elipe, P.; Manners, I. *Chem. Rev.* **1999**, *99*, 1515. (c) Manners, I. *Science* **2001**, *294*, 1664.
(12) Yajima, S.; Omori, M. *Nature* **1977**, *267*, 823.

Scheme 1. Synthesis of Cobalt-Clusterized Polyferrocenylsilane (Co−PFS) (2)
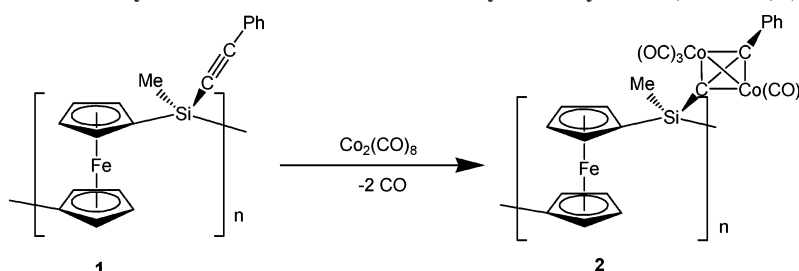
and Keller have converted linear ferrocenylene-siloxyl-diacetylene polymers to Fe-containing ceramics with high thermal and oxidative stabilities.[13] Polyferrocenylsilanes (PFS), which are readily available via ring-opening polymerization (ROP) techniques,[14] yield ceramic materials containing magnetic α-Fe NPs embedded in a $C/SiC/Si_3N_4$ matrix on pyrolysis at 600−1000 °C.[15−18] Tang and co-workers have prepared ceramics containing $\alpha\text{-}Fe_2O_3$ nanocrystals from a hyperbranched PFS precursor.[19,20] Using PFS block copolymer precursors in thin films, Lastella et al.[21] and Hinderling et al.[22] have independently prepared patterned Fe-based NPs from phase-separated PFS nanodomains that can act as catalysts for carbon nanotube growth. In addition, Lu et al. have used this type of approach to pattern single-walled carbon nanotubes with well-defined diameters at specific locations on a substrate.[23]

Cobalt-containing polymers have also been studied for the generation of Co-based NPs. For example, Corriu and co-workers reported the thermolysis of polycarbosilanes with cobalt carbonyl groups that yielded a cobalt-containing ceramic material in high yield.[24] Recently, Tang and co-workers also reported hyperbranched polyynes containing Co clusters, which were pyrolyzed to yield materials with soft ferromagnetic properties.[25] Grubbs and co-workers fabricated carbon nanotubes and Co-based NPs simultaneously by pyrolyzing well-defined diblock copolymers

containing Co cluster substituents.[26] In addition, Bunz and co-workers reported that the pyrolysis of a dicobalthexa-carbonyl-complexed poly(*p*-phenyleneethynylene) yields micrometer-sized carbon−cobalt spheres.[27,28]

For many applications of metal NPs such as uses in nanoelectronics, magnetic data storage, and catalysis, it is essential to control their composition and their density per unit area as well as their spatial location. Most metallopolymers studied as metal NP precursors possess relatively low loadings of metal atoms.[29] In addition, most metal-containing polymers studied to date contain only a single metal, rendering metal alloy NPs inaccessible. This shortcoming motivated our group to prepare PFS derivatives with pendant acetylenic substituents (**1**) that can be clusterized with various metals such as Co, Ni, and Mo.[30−33] These polymers contain a large number of metal atoms per repeat unit, which results in metal contents of up to 30 wt %.[33] As these metallopolymers can be readily patterned using techniques such as electron-beam lithography,[34] UV photolithography,[35] and soft lithography,[36] they offer the prospect of accessing patterned arrays of metal and metal alloy NPs for device and catalytic applications. In recent preliminary studies, we focused on the bulk pyrolysis of the cobalt clusterized PFS polymer Co−PFS (**2**; Scheme 1).[31] Pyrolysis of Co−PFS (**2**) under N_2 at 600 °C and 900 °C for 12 h afforded magnetic ceramics in

(13) Houser, E. J.; Keller, T. M. *Macromolecules* **1998**, *31*, 4038.
(14) (a) Manners, I. *Chem. Commun.* **1999**, 857. (b) Manners, I. *Can. J. Chem.* **1998**, *76*, 371. (c) Kulbaba, K.; Manners, I. *Macromol. Rapid Commun.* **2001**, *22*, 711.
(15) Tang, B.-Z.; Petersen, R.; Foucher, D. A.; Lough, A. J.; Coombs, N.; Sodhi, R.; Manners, I. *J. Chem. Soc., Chem. Commun.* **1993**, 523.
(16) Petersen, R.; Foucher, D. A.; Tang, B.-Z.; Lough, A. J.; Raju, N. P.; Greedan, J. E.; Manners, I. *Chem. Mater.* **1995**, *7*, 2045.
(17) MacLachlan, M. J.; Ginzburg, M.; Coombs, N.; Coyle, T. W.; Raju, N. P.; Greedan, J. E.; Ozin, G. A.; Manners, I. *Science* **2000**, *287*, 1460.
(18) Ginzburg, M.; MacLachlan, M. J.; Yang, S. M.; Coombs, N.; Coyle, T. W.; Raju, N. P.; Greedan, J. E.; Herber, R. H.; Ozin, G. A.; Manners, I. *J. Am. Chem. Soc.* **2002**, *124*, 2625.
(19) Sun, Q.; Lam, J. W. Y.; Xu, K.; Xu, H.; Cha, J. A. K.; Wong, P. C. L.; Wen, G.; Zhang, X.; Jing, X.; Wang, F.; Tang, B. Z. *Chem. Mater.* **2000**, *12*, 2617.
(20) Sun, Q.; Xu, K.; Peng, H.; Zheng, R.; Häussler, M.; Tang, B. Z. *Macromolecules* **2003**, *36*, 2309.
(21) Lastella, S.; Jung, Y. J.; Yang, H. C.; Vajtai, R.; Ajayan, P. M.; Ryu, C. Y.; Rider, D. A.; Manners, I. *J. Mater. Chem.* **2004**, *14*, 1791.
(22) Hinderling, C.; Keles, Y.; Stöckli, T.; Knapp, H. F.; de los Arcos, T.; Oelhafen, P.; Korczagin, I.; Hempenius, M. A.; Vancso, G. J.; Pugin, R.; Heinzelmann, H. *Adv. Mater.* **2004**, *16*, 876.
(23) Lu, J. Q.; Kopley, T. E.; Moll, N.; Roitman, D.; Chamberlin, D.; Fu, Q.; Liu, J.; Russell, T. P.; Rider, D. A.; Manners, I.; Winnik, M. A. *Chem. Mater.* **2005**, *17*, 2227.
(24) Corriu, R. J. P.; Devylder, N.; Guerin, C.; Henner, B.; Jean, A. *J. Organomet. Chem.* **1996**, *509*, 249.
(25) Häussler, M.; Zheng, R.; Lam, J. W. Y.; Tong, H.; Dong, H.; Tang, B. Z. *J. Phys. Chem. B* **2004**, *108*, 10645.

(26) (a) Mîinea, L. A.; Sessions, L. B.; Ericson, K. D.; Glueck, D. S.; Grubbs, R. B. *Macromolecules* **2004**, *37*, 8967.(b) Grubbs, R. B. *J. Polym. Sci., Part A: Polym. Chem.* **2005**, *43*, 4323.
(27) Scholz, S.; Leech, P. J.; Englert, B. C.; Sommer, W.; Weck, M.; Bunz, U. H. F. *Adv. Mater.* **2005**, *17*, 1052.
(28) Other metal NPs, such Au and Ru NPs, can also be prepared from metallized polymer precursors via electron beam treatment; see: (a) Corbierre, M. K.; Beerens, J.; Lennox, R. B. *Chem. Mater.* **2005**, *17*, 5774. (b) Johnson, B. F. G.; Sanderson, K. M.; Shephard, D. S.; Ozkaya, D.; Zhou, W. Z.; Ahmed, H.; Thomas, M. D. R.; Gladden, L.; Mantle, M. *Chem. Commun.* **2000**, 1317. (c) Zhang, T.; Druvin, M.; Harvey, P. D. *Inorg. Chem.* **1999**, *38*, 957.
(29) Rare exceptions: (a) Lucas, N. T.; Humphrey, M. G.; Rae, A. D. *Macromolecules* **2001**, *34*, 6188. (b) Also ref 28b.
(30) Berenbaum, A.; Lough, A. J.; Manners, I. *Organometallics* **2002**, *21*, 4415.
(31) Berenbaum, A.; Ginzburg-Margau, M.; Coombs, N.; Lough, A. J.; Safa-Sefat, A.; Greedan, J. E.; Ozin, G. A.; Manners, I. *Adv. Mater.* **2003**, *15*, 51.
(32) Chan, W. Y.; Berenbaum, A.; Clendenning, S. B.; Lough, A. J.; Manners, I. *Organometallics* **2003**, *22*, 3796.
(33) Chan, W. Y.; Berenbaum, A.; Clendenning, S. B.; Lough, A. J.; Manners, I.; Aouba, S.; Ruda, H. E. *J. Am. Chem. Soc.* **2005**, *127*, 1765.
(34) Clendenning, S. B.; Aouba, S.; Rayat, M. S.; Grozea, D.; Sorge, J. B.; Brodersen, P. M.; Sodhi, R. N. S.; Lu, Z.-H.; Yip, C. M.; Freeman, M. R.; Ruda, H. E.; Manners, I. *Adv. Mater.* **2004**, *16*, 215.
(35) Cheng, A. Y.; Clendenning, S. B.; Yang, G. C.; Lu, Z.-H.; Yip, C. M.; Manners, I. *Chem. Commun.* **2004**, 780.
(36) Clendenning, S. B.; Fournier-Bidoz, S.; Pietrangelo, A.; Yang, G. C.; Han, S. J.; Brodersen, P. M.; Yip, C. M.; Lu, Z.-H.; Ozin, G. A.; Manners, I. *J. Mater. Chem.* **2004**, *14*, 1686.

Pyrolysis of Highly Metallized Polymers

Chem. Mater., Vol. 18, No. 10, 2006 2593

72 and 59% yield, respectively. The analysis of the ceramics by transmission electron microscopy (TEM) with elemental mapping as well as powder X-ray diffraction (PXRD) analysis revealed that the ceramics contain CoFe alloy NPs embedded in an essentially amorphous SiC/C ceramic matrix. The magnetic properties of the ceramics could be tuned between the superparamagnetic and the ferromagnetic states by increasing the pyrolysis temperature from 600 to 900 °C, which increased the size of the CoFe alloy NPs present in the material.

To date, virtually all studies of the pyrolytic conversion of metallopolymers to metal-containing ceramics have focused on the use of metallopolymer precursors in the bulk state. In contrast, reports on the preparation of ceramic thin films are extremely rare.[37] In this paper, we present in-depth studies on the pyrolysis of films of Co−PFS (**2**) to form magnetic ceramic thin films. This work is an essential prerequisite for the potential use of such metallized polymer precursors in the fabrication of spintronic devices such as nanogranular in-gap structures[38] and in catalysis.[39] In the present study, our focus was on the influence of pyrolysis temperature on the ceramic film thickness and morphology, the NP size and size distribution, composition, and magnetic properties.

Experimental Section

Polymer Synthesis. Co−PFS (**2**) was synthesized according to literature procedures.[30,31] Approximately 85% of the acetylene moieties in PFS (**1**) were clusterized with $Co_2(CO)_8$ as calculated using the integrals of the methyl resonances in the ^1H NMR spectrum. The molecular weight of the PFS (**1**) prior to clusterization was determined to be $M_n = 95\,200$ g/mol (polydispersity index = 3.15) by GPC.[31]

Substrate Preparation. Silicon (100) substrates were purchased from Wafer World, Inc., and cleaned by sonication for 10 min in CH_2Cl_2, 2-propanol, "piranha" solution (30% H_2O_2/concentrated H_2SO_4, 1:3 vol %, CAUTION!) and deionized water prior to drying in a jet of filtered air.

Spin-Coating. Co−PFS was dissolved in toluene (3.6 wt %) and gave a brown solution that was filtered with a Whatman 13 mm GD/X nylon syringe filter (0.45 μm pore size) immediately prior to spin-coating. The about 9 cm² Si wafer was coated with the polymer solution and immediately accelerated to 600 rpm for 18 s, followed by 60 s at 1000 rpm.

Pyrolysis. Spin-coated films of Co−PFS were placed in a quartz boat inside a quartz tube in a three-zone Lindberg tube furnace. The tube was purged with a prepurified mixture of N_2/H_2 atmosphere (92%/8%) for 30 min (1 L·min^{-1}) prior to lowering the flow to about 50 mL·min^{-1} for pyrolysis. The temperature of the tube furnace was increased at a rate of 15 °C·min^{-1} to the desired temperature and then held constant for 2 h prior to cooling to ambient temperature. The pyrolysis of Co−PFS (**2**) at each temperature was repeated several times to confirm reproducibility.

Ellipsometry. A Sopra (GES-5) spectroscopic ellipsometer acquired Ψ and Δ data from 0.62 to 4.00 eV, using the analyzer in

(37) (a) Li, Y. M.; Zheng, Z. M.; Reng, C. Y.; Zhang, Z. J.; Gao, W.; Yang, S. Y.; Xie, Z. M. *Appl. Organomet. Chem.* **2003**, *17*, 120. (b) Clendenning, S. B.; Han, S.; Coombs, N.; Paquet, C.; Rayat, M. S.; Grozea, D.; Brodersen, P. M.; Sodhi, R. N. S.; Yip, C. M.; Lu, Z.-H.; Manners, I. *Adv. Mater.* **2004**, *16*, 291.
(38) Jalil, M. B. A. *IEEE Trans. Magn.* **2002**, *38*, 2613.
(39) Duvenhage, D. J.; Coville, N. J. *Appl. Catal., A* **1997**, *153*, 43.
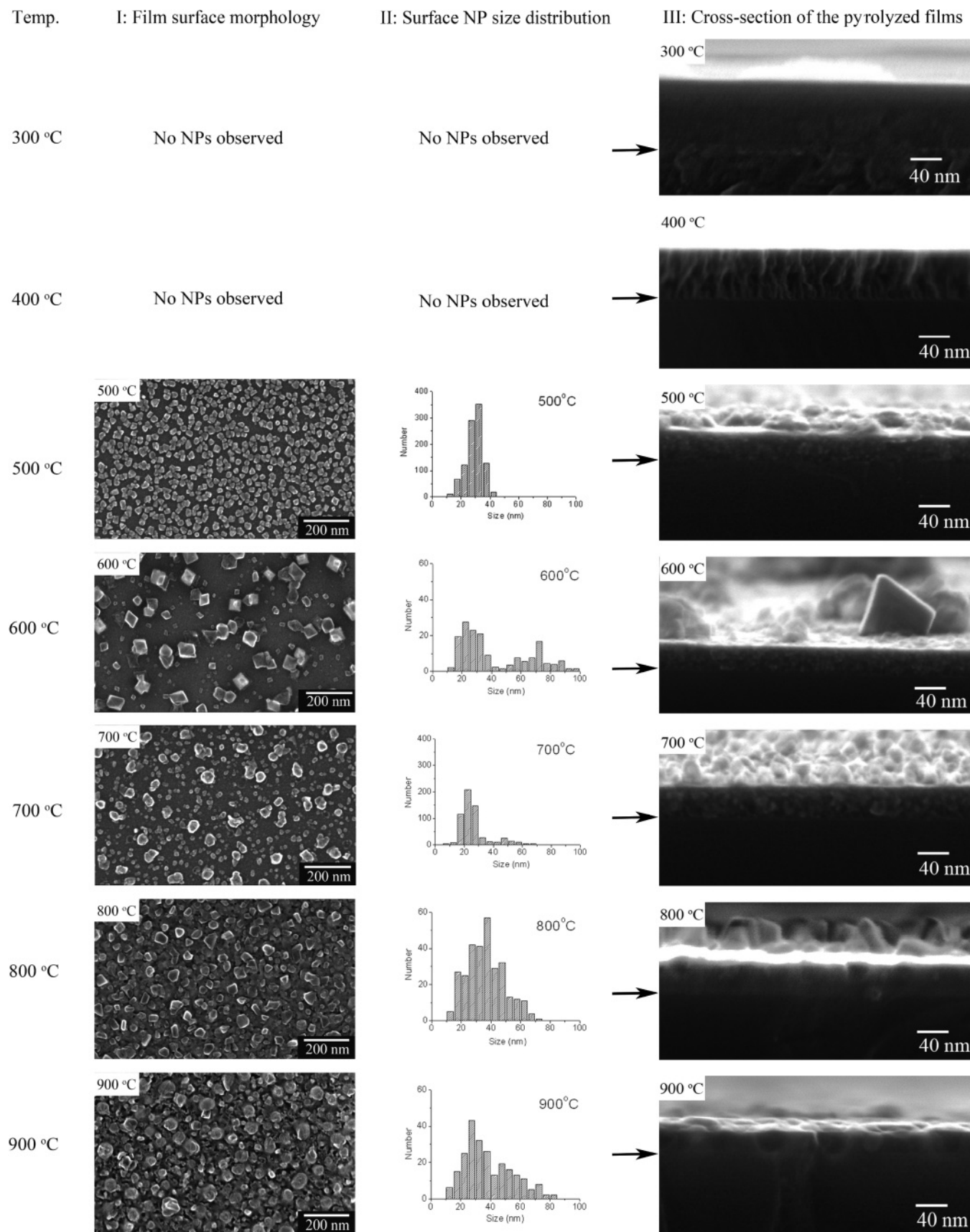
a previous tracking mode and with the integration time for each data point determined by either the minimum threshold of 2 000 000 detector counts or 10 s. A Levenberg−Marquardt algorithm was used to fit a three-layer model of the polymer films to the experimentally acquired $\cos(2\Psi)/\sin(2\Psi)\cos(\Delta)$ curves. The three-layer model consisted of a homogeneous crystalline Si substrate, a 2 nm thick layer of SiO_2, and the polymer layer which was described by a Cauchy dispersion law with one superimposed Lorentz peak.

Scanning Electron Microscopy (SEM). SEM images were obtained using a Hitachi S-5200 scanning electron microscope operating at 30 kV. The cross-sectional samples were prepared by breaking the samples in the middle, stabilizing the samples vertically with SEM substrates, and then viewing them on a 2° angle in the scanning electron microscope.

Size Distribution Measurement. The maximum diameter was recorded as the size of particles. For each sample, all particles in one 1.15 μm × 0.8 μm picture as shown in the SEM images (Figure 1, series I) were measured and counted.

Transmission Electron Microscopy. TEM images were obtained with a Hitachi HD-2000 scanning transmission electron microscope operating at 200 kV.

Energy Dispersive X-ray (EDX) Elemental Analysis. EDX was performed on a 11.5 μm × 8 μm area of the sample using a Hitachi S-5200 scanning electron microscope operating at 30 kV with a windowless X-ray detector.

EDX Elemental Mapping Analysis. NPs prepared at 600 °C were peeled off from the film surface onto the TEM grid. Maps and images were recorded using a Hitachi HD-2000 scanning transmission electron microscope operating at 200 kV with a windowless X-ray detector.

X-ray Photoelectron Spectroscopy (XPS). The sample surface was analyzed using a PHI 5500 ESCA system. The XPS spectra were generated by a monochromated Al Kα source with a photon energy of 1486.7 eV and were recorded at a photoelectron takeoff angle of 45°, giving a ca. 5−6 nm detection depth. The analysis area was 800 μm in diameter. The peak positions were aligned and corrected for charge effects on the basis of the adventitious C 1s peak position at 284.8 eV. For the depth-profiling analysis, an Ar$^+$ ion beam of 3 keV of energy at 60° was used. The sputter rate was calibrated for SiO_2/Si structures.

Scanning Probe Microscopy. Tapping mode atomic force microscopy (AFM) was performed on a Digital Instruments Multimode IIIa Nanoscope system using Nanoprobe MESP magnetic coated scanning probes and nanosensor (PPP-NCH-50). The samples were mounted on steel sample pucks and imaged in air using an E-scanner (nominal maximum scan size of 14.6 μm × 14.6 μm) with the scan rate of 1−2 Hz. All the images were collected at a resolution of 512 × 512 pixel data sets. Image analysis was performed using the Digital Instruments Nanoscope software (4.42r9). Images were processed using the same software and were flattened and plane-fitted.

Magneto-Optic Kerr Effect (MOKE) Measurements. The samples were placed between the poles of a small electromagnet, such that the applied field was in the plane of the substrate and parallel to samples' surface. Probe light at 532 nm from an intracavity-doubled continuous-wave Nd:YVO$_4$ diode-pumped solid-state laser (Spectra Physics Millennia) was incident at 20° off the normal, with the plane of incidence containing the *x* axis. With the laser output attenuated to 43 mW, 3 mW was split-off and directed, through a variable beam attenuator, to a reference photodiode used to subtract common-mode laser noise from the Kerr signal. The remaining light was focused toward the specimen using a 0.5 m focal length plano-convex lens, positioned such that the sample was not at the beam waist but at a location where the beam diameter

Temp.   I: Film surface morphology   II: Surface NP size distribution   III: Cross-section of the pyrolyzed films

300 °C   No NPs observed   No NPs observed

400 °C   No NPs observed   No NPs observed

Figure 1. Vertical view SEM images (series I), surface particle size distributions (series II), and cross-sectional SEM images (series III) for Co−PFS (**2**) thin films pyrolyzed at 300, 400, 500, 600, 700, 800, and 900 °C. The original film thickness before pyrolysis was about 200 nm. The arrows in series III indicate the interface of the Si substrate and the pyrolyzed film.

was roughly 200 μm (as determined by in situ inspection through a long working distance microscope). The beam at this fluence was a "noninvasive" probe, as confirmed by reference measurements

showing no alteration of the magnetic behavior at up to 10× higher fluence, under a tighter focus and with higher initial laser power. The incident beam was p-polarized and "scrubbed" to high linear

purity (1:105) by a calcite polarizer. The polarization change of the reflected light was determined by the differential transmittance through a nearly orthogonal (offset by 1°) calcite polarization analyzer.

Results and Discussion

Samples of the Co-clusterized polyferrocenylsilane Co−PFS (**2**) were prepared by previously reported methods (Scheme 1).[31] The clusterization ratio of the acetylene groups in PFS (**1**) with $Co_2(CO)_8$ was shown to be about 85% by ^{1}H NMR spectroscopy. Gel permeation chromatography showed that the precursor polymer PFS (**1**) was of high molecular weight. PFS (**1**) was prepared by ROP of the corresponding strained, acetylene-substituted [1]ferrocenophane using a Pt catalyst.[30]

The pyrolysis of thin films of Co−PFS (**2**; thickness, about 200 nm, on silicon substrate) under a N_2/H_2 atmosphere (92%/8%) was investigated at different temperatures. The reductive atmosphere was used to minimize the oxidation of the resulting ceramics and metal NPs by traces of oxygen and moisture contained in the N_2 gas. Samples of the Co−PFS (**2**) thin films were pyrolyzed for 2 h at seven temperatures (300, 400, 500, 600, 700, 800, and 900 °C). In this range of temperatures the color of the films was found to change with increasing pyrolysis temperature from dark pink to light yellow when observed orthogonal to the film surface. These interference colors offered preliminary evidence for changes in the films such as thickness, coarseness, and surface particle size. Detailed studies of the ceramic films were carried out by SEM, AFM, TEM, EDX, SAED (selected-area electron diffraction), XPS, and MOKE. The pyrolysis of Co−PFS (**2**) at each temperature was repeated several times to confirm reproducibility.

1. Morphology and Structure of the Thin Ceramic Films. *(a) Analysis by SEM.* The dependencies of the surface morphology and the structure of ceramic films on the pyrolysis temperatures (300−900 °C) were investigated by SEM (vertical views in series I of Figure 1 and cross-sectional views in series III of Figure 1). In addition, the surface particle size distributions of the films obtained from the respective SEM vertical view images are given in series II of Figure 1. Excellent reproducibility of the pyrolysis experiments was observed by SEM. Cracks caused by volume shrinkage during pyrolysis were not detected by SEM for the ceramic films under any conditions.

For polymer films pyrolyzed at 300 and 400 °C, no surface NPs were discernible. The SEM cross-sectional image (Figure 1, series III at 300 °C) for the 300 °C sample showed a homogeneous ca. 86 nm thick polymer/ceramic layer on the Si substrate. The film surface was smooth, and no particles on the surface or in the underlying layer were observed by SEM. Previous thermogravimetric analysis studies on bulk Co−PFS (**2**) under a N_2 atmosphere showed that weight loss starts at a temperature of about 80 °C and levels off at 320 °C.[31] This corresponds to the loss of the labile carbonyl ligands.[24] Above this temperature (from 350 to 900 °C), limited weight loss (<10%) was detected. In the case of the pyrolysis of Co−PFS (**2**) thin films, the film contraction from the original thickness of about 200 nm to
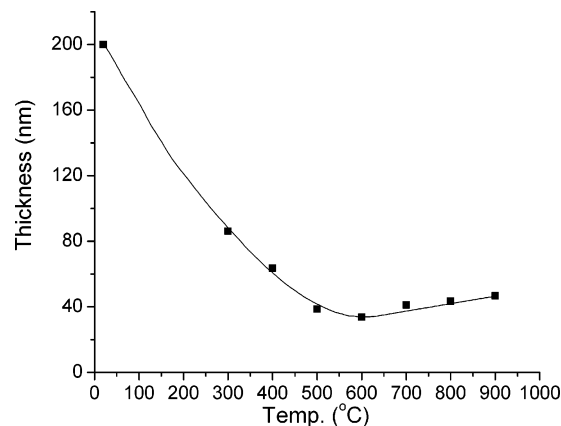

Figure 2. Plot of film thickness obtained from cross-sectional SEM vs pyrolysis temperature (see Figure 1, series III).

86 nm (see also Figure 2) after pyrolysis at 300 °C for 2 h could be attributed to the loss of CO ligands, to the loss of any residual toluene used as solvent for spin-coating, and to densification during the conversion from polymer to ceramic. At the pyrolysis temperature of 400 °C, a comparatively thinner film (ca. 64 nm) was obtained (Figure 1, series III at 400 °C, and Figure 2), presumably due to the further loss of CO and low molecular weight compounds formed by fragmentation and depolymerization reactions and further densification during the pyrolysis process. No particles were observed on the surface or in the underlying layer of this film either.

Figure 1, series I at 500 °C, revealed that a pyrolysis temperature of 500 °C resulted in a film surface densely covered by well-faceted NPs. These NPs exhibited an average diameter of 29.5 ± 5.7 nm with a fairly narrow and monomodal size distribution (Figure 1, series II at 500 °C). The NPs were randomly dispersed on a smooth ceramic layer with short interparticle distances. Because of the high particle density on the surface, some of the NPs appeared to form multiparticle aggregates. The cross-sectional SEM image (Figure 1, series III at 500 °C) showed large particles on a smooth film surface, while much smaller particles of rather uniform size of about 4 nm were visible in the ceramic layer below the film surface. This result indicated that, during the pyrolysis process, release of metal atoms from the thermolyzed metallopolymer and metallic crystallization occurred both on the surface and in the underlying layer of the ceramic films. The larger size of the NPs at the ceramic surface was presumably a consequence of the more rapid diffusion possible at the two-dimensional phase boundary which facilitates metal atom agglomeration.

The SEM image (Figure 1, series I at 600 °C) was obtained for the ceramic film prepared at 600 °C. Particles were found to be located on top of the ceramic layer but in a much lower density compared to those of the sample prepared at 500 °C. Furthermore, the particle size distribution at 600 °C was bimodal (Figure 1, series II at 600 °C). The average sizes of large and small particles on the surface were about 70 and 25 nm, respectively. Most of the surface particles were well-faceted, square-based bipyramid-shaped or generic-prism-shaped crystals. Some multiparticle aggregates formed by small and large particles were also observed in this com-

posite. The film thickness of about 34 nm (Figure 1, series III at 600 °C) was lower than that of the sample prepared at 500 °C. The large faceted surface particles were obviously embedded into the ceramic layer. Similar to the film prepared at 500 °C, there were more uniform and small NPs located in the underlying layer with an average size of about 4 nm.

The SEM image of the film pyrolyzed at 700 °C (Figure 1, series I at 700 °C) revealed a bimodal particle size distribution, although the bimodality was much less pronounced than in the sample pyrolyzed at 600 °C. By increasing of the pyrolysis temperature from 600 to 700 °C the morphology of the surface particles changed from faceted to a more rounded shape. An increased number of small particles were observed on the surface, and the percentage of large particles was significantly decreased (Figure 1, series II at 700 °C). The mean size of the small surface particles was found to be around 25 nm and was, therefore, similar to that of the sample pyrolyzed at 600 °C. The cross-sectional SEM image of the film pyrolyzed at 700 °C (Figure 1, series III at 700 °C) revealed that the size of the NPs in the underlying layer was increased compared to the NPs in the 600 °C sample. The formation of large NPs could be attributed to enhanced metal atom mobility in the matrix above 700 °C. Presumably above 600 °C Si−C and C−C bond cleavage readily occurred, facilitating rearrangements in the matrix and metal atom mobility. Similar phenomena were apparent in our previous pyrolysis study of highly cross-linked PFS networks.[18]

A very rough surface resulted after pyrolysis at 800 °C (Figure 1, series I and series III at 800 °C). Generic prism-shaped particles were embedded in the ceramic layer. The surface particle size distribution was very broad with an average size of 36.5 ± 12.5 nm (Figure 1, series II at 800 °C). No small particles were visible in the ceramic layers prepared at 800 °C and above. In addition, some hollows were observed in the ceramic layer. Because no hollows are present in the SEM image for the same sample, their formation can be attributed to the loss of large faceted particles during the sample preparation for SEM cross-sectional investigations. The observation of hollows confirmed that the removed surface NPs were embedded in the ceramic layer.

With a further increase to the highest pyrolysis temperature examined (900 °C) (Figure 1, series I and II at 900 °C), the mean surface NP size increased to 40.5 ± 14.8 nm and the size distribution became even broader. Compared to the particles in the 800 °C sample, the prism shape was lost at 900 °C and more rounded morphologies dominate. Cross-sectional SEM (Figure 1, series III at 900 °C) revealed a relatively flat surface at 900 °C. The height of the particles protruding from the surface was decreased, and deeper and more rounded hollows in the ceramic layer were observed. This result indicated that the particles are deeply embedded in the ceramic layer with an increase of size and a shape tending toward spheres rather than prisms.

The thickness of the ceramic layers was determined from the cross-sectional SEM images (Figure 1, series III). A plot of the ceramic film thickness versus pyrolysis temperature is shown in Figure 2. The plot shows that the film thickness

decreased from about 86 to 34 nm with an increase in the pyrolysis temperature from 300 to 600 °C and remained rather constant at about 41−47 nm between 700 and 900 °C. This result indicated that thermal conversion of the polymer to ceramic with the concomitant loss of small amounts of low molecular weight compounds and densification were complete at 600 °C. The slight increase in film thickness above 600 °C may be attributed to an increase of ceramic yield due to the enhanced formation of SiC and graphite catalyzed by Fe and Co at these temperatures.[40,41] Indeed, in our previous pyrolysis study of highly cross-linked PFS networks, graphite was observed to be formed initially at 700 °C, and more graphite was apparent with increasing temperature.[18]

(b) AFM Studies. The surface morphologies of the ceramic films pyrolyzed at 500, 600, and 900 °C were also investigated by AFM. Figure 3a showed that the ceramic film pyrolyzed at 500 °C was densely covered by NPs. These particles showed a monomodal size distribution with an average size of 36.8 ± 6.6 nm, which was larger than that determined by SEM. This difference of particle size between the SEM and AFM measurements was expected due to convolution of the image with the shape of the tip in the latter. The cross-sectional analysis (Figure 3a, bottom) gave an average height for the NPs of 18.5 ± 3.8 nm. The difference between the average height and size of these NPs indicated that, on average, very approximately around half of any NP was embedded in the ceramic layer.

The AFM height image and cross-sectional analysis of the ceramic thin film formed after pyrolysis at 600 °C for 2 h are presented in Figure 3b. The AFM images show the formation of large (74.1 ± 11.8 nm) and small particles (36.5 ± 6.8 nm) on the film surface as found by SEM. The cross-sectional analysis indicated that the average heights of the large and small particles protruding from the surface were 63.6 ± 8.7 nm and 23.5 ± 5.3 nm, respectively.

A very flat ceramic surface was observed in the AFM height image and cross-sectional analysis of the ceramic thin film pyrolyzed at 900 °C (Figure 3c). The average height of particles above the surface was only 6.8 ± 2.6 nm, which was considerably less than for the other investigated samples that were prepared below 900 °C. A careful investigation of the height image showed that most particles were deeply embedded in the ceramic layer and only the top part of them could be detected by AFM. Thus, the width and height of the particles could not be estimated with accuracy.

(c) Studies by TEM. To further investigate the structure of the NPs within the thin ceramic films, a TEM study was carried out on a representative film prepared on a Si_3N_4 covered TEM grid.

Figures 4a,b show the SEM and TEM images, respectively, for the same area of the ceramic film obtained at 600 °C after 2 h. The SEM image in Figure 4a was similar to that of the ceramic film prepared on the Si(100) substrate under

(40) Rao, C. N. R.; Sen, R.; Satishkumar, B. C.; Govindaraj, A. *Chem. Commun.* **1998**, 1525.
(41) Corriu, R. J. P.; Enders, M.; Huille, S.; Lutsen, L.; Moreau, J. J. E. In *Applications of Organometallic Chemistry in the Preparation and Processing of Advanced Materials*; Harrod, J. F.; Laine, R. M., Eds.; Kluwer: Dordrecht, 1995.
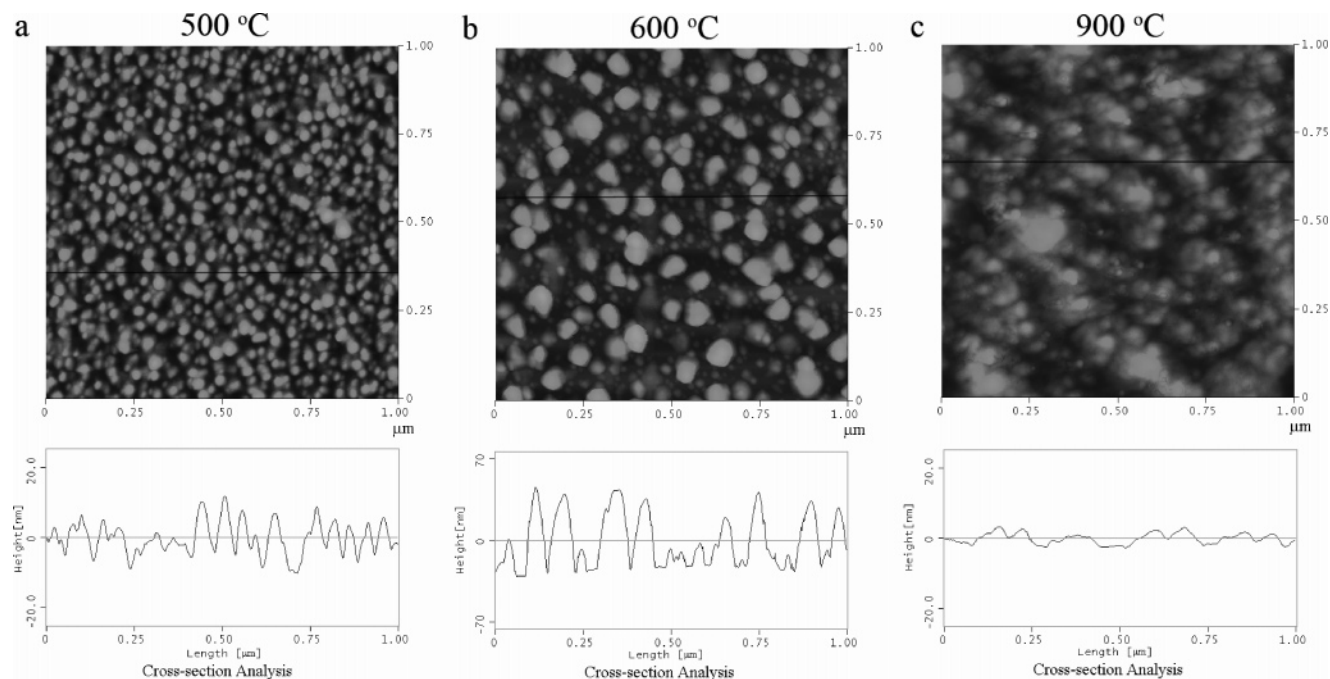
Pyrolysis of Highly Metallized Polymers

Chem. Mater., Vol. 18, No. 10, 2006 2597

Figure 3. AFM height images (top) and cross-sectional analysis images (below) of Co−PFS (**2**) thin films pyrolyzed at (a) 500, (b) 600, and (c) 900 °C for 2 h.
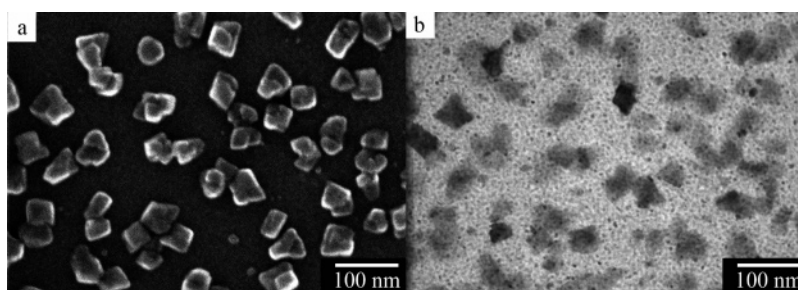

Figure 4. (a) SEM and (b) TEM images of the same area of Co−PFS (**2**) thin films pyrolyzed at 600 °C for 2 h.

the same conditions (Figure 1, series I at 600 °C). The surface was covered with large bipyramidal NPs and multiparticle aggregates. The TEM image (Figure 4b) of the same area shows these large surface particles (as seen in the SEM image in Figure 4a) as well as the much smaller particles inside the ceramic matrix. The average size of the small particles in the underlying layer was found to be about 4.1 ± 0.6 nm, which was consistent with the particle size determined from the SEM cross-sectional study of the film prepared at the same conditions (Figure 1, series III at 600 °C). The appearance of "darker" and "brighter" NPs resulted from an enhanced diffraction contrast due to the particles' orientation with respect to the electron beam.[42] The presence of dark dots in the individual large surface NPs indicated that small NPs were located beneath the surface ceramic layer. Apart from the small dark dots in the image, each large particle had near-uniform contrast which indicated that the particles had a single-crystal core.[42]

2. Composition of the Thin Ceramic Films and NP Structure. *(a) Elemental Analysis and Mapping by EDX.* EDX analysis was used to investigate the chemical compositions of the ceramic films. Table 1 lists the composition of

Table 1. EDX Results of Element Atomic Content for the Sample Pyrolysis from 300 to 900 °C

element atomic %	300 °C	400 °C	500 °C	600 °C	700 °C	800 °C	900 °C
C	5.42	4.39	5.10	4.24	5.29	4.61	5.18
O	6.28	5.64	6.60	5.68	4.54	6.36	5.45
Si	87.54	88.63	87.56	89.38	89.51	88.42	88.80
Fe	0.23	0.19	0.23	0.22	0.20	0.17	0.18
Co	0.53	0.43	0.50	0.48	0.46	0.44	0.40

the ceramic films at the applied pyrolysis temperatures. The EDX analyses revealed that the contents of Fe and Co atoms in the ceramic films were in the range of 0.17−0.23% and 0.40−0.50%, respectively. On the basis of an estimated error of ±10% for the content of Fe and ±5% for the content of Co, the approximate ratio of Fe/Co was about 1:2.2 which was fairly close to the value of 1:1.7 for the Co−PFS polymer precursor (**2**) based on the percentage of Co clusterization (ca. 85%).[43]

Because the EDX experiments were performed on ceramic films supported on Si substrates, the EDX values for Si did

(42) Murray, C. B.; Sun, S. H.; Gaschler, W.; Doyle, H.; Betley, T. A.; Kagan, C. R. *IBM J. Res. Dev.* **2001**, *45*, 47.

(43) This difference of the Fe/Co ratio may be caused by the more pronounced loss of Fe atoms than that of Co atoms during pyrolysis. It is known that during pyrolysis of polyferrocenyldimethylsilane, Fe-containing orange-colored volatile byproducts are formed above 350 °C.[16] Orange-colored byproducts have also been observed in the pyrolysis tube during pyrolysis of bulk Co−PFS.
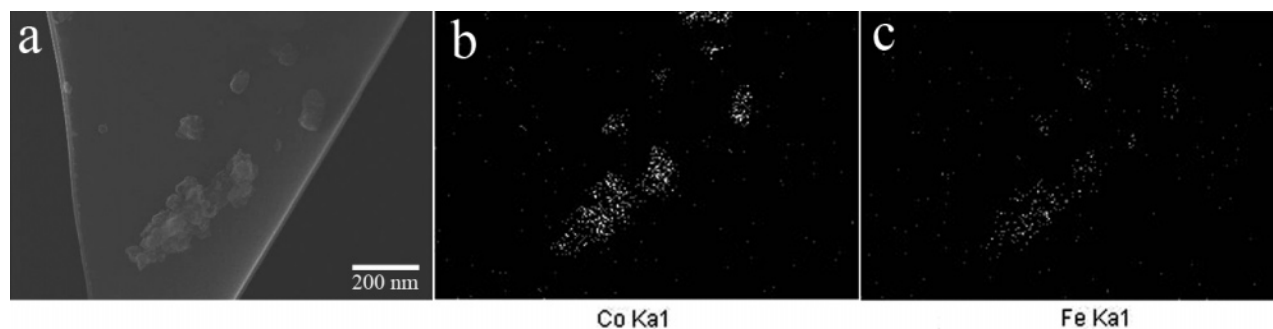
Figure 5. (a) TEM image of CoFe alloy NPs from Co−PFS (**2**) thin films pyrolyzed at 600 °C for 2 h and corresponding element maps for (b) Co and (c) Fe.
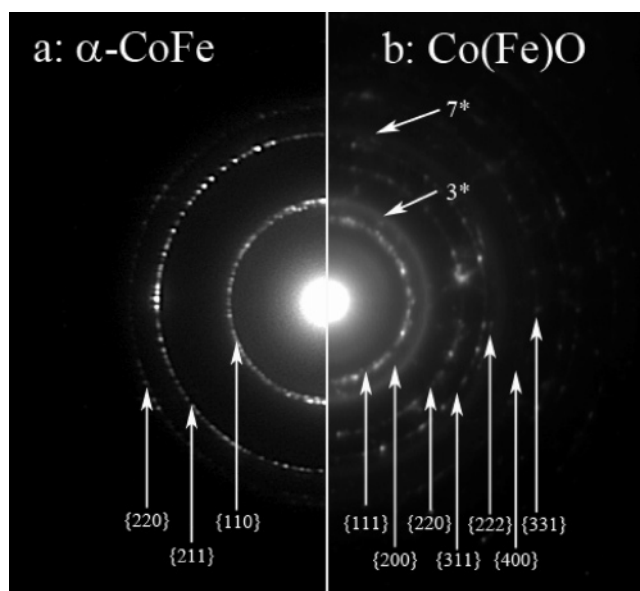

Figure 6. SAED patterns for Co−PFS (**2**) thin films pyrolyzed at 500 °C: (a) α-CoFe phase pattern and (b) superposition of α-CoFe phase pattern (arrow-labeled broad lines) and Co(Fe)O phase pattern.

Table 2. Phase Identification by Electron Diffraction Data for the Sample Pyrolyzed at 500 °C: (a) α-CoFe Phase and (b) Co(Fe)O Phase

	d (Å), measured[a]		Miller indices			d (Å), standard data		
	a	b	CoFe	CoO	FeO	CoFe	CoO	FeO
1		2.48		{111}	{111}		2.4612	2.4900
2		2.14		{200}	{200}		2.1315	2.1530
3	2.02	2.03[b]	{110}			2.0202		
4		1.51		{220}	{220}		1.5072	1.5230
5		1.29		{311}	{311}		1.2853	1.2990
6		1.24		{222}	{222}		1.2306	1.2430
7	1.17	1.16[b]	{211}			1.1664		
8		1.05		{400}	{400}			1.0770
9	1.00	1.01[b]	{220}			1.0101		
10		0.98		{331}	{331}			0.9880

[a] Measurement error ±0.05 Å. [b] Additional diffractions corresponding to the α-CoFe phase.

(b) SAED Studies. To investigate the structure of the metal NPs in more detail, SAED experiments were performed on the films prepared at 500 to 900 °C. Two types of SAED patterns were observed at different locations on the same sample prepared at 500 °C. These are shown in Figure 6a,b. The diffraction pattern in Figure 6a exhibited three diffraction rings with d spacings of 2.02, 1.17, and 1.00 Å from the inside to the outside. These three d spacings agreed well with the d spacings of the α-CoFe phase: {110} ($d_{\{110\}}$ = 2.0202 Å), {211} ($d_{\{211\}}$ = 1.1664 Å), and {220} ($d_{\{220\}}$ = 1.0101 Å).[45] The measured d spacings and standard crystallographic data are listed in Table 2. From the binary CoFe phase diagram, an α-CoFe phase exists with a disordered body-centered cubic (bcc) structure and a lattice parameter of a = 2.857 Å.[46] This α-CoFe phase has an A1-bcc structure, in which Co atoms randomly replace Fe atoms in the bcc α-Fe lattice. This type of crystal structure had also been indicated in our previous preliminary study on the pyrolysis of bulk samples of Co−PFS (**2**) as determined by PXRD.[31] Thus, the three diffraction rings could be identified as {110}, {211}, and {220} diffractions of an α-CoFe phase, which confirmed that an α-CoFe phase existed in the ceramic film obtained at 500 °C.

As discussed above, the surface metal NPs can be easily oxidized by O_2 in air during the storage and process.[44] Thus, it is reasonable to expect that a phase of metal oxides would be present. For the SAED pattern in Figure 6b the d-spacing

not provide useful information on the film composition. In addition, the EDX value for oxygen could be attributed to a thin oxide layer on top of Si substrates, although it is likely that a contribution also arises from the reactions of O_2 and moisture with the surfaces of the ceramic films during workup and storage of the samples. It is well-established that many metal NPs are oxidized immediately on exposure to air.[44]

EDX mapping analysis was applied to determine whether the NPs contained both Co and Fe or were only composed of a single metal. The TEM image in Figure 5a shows the metal particles that were peeled off from the surface of the ceramic film pyrolyzed at 600 °C. Figure 5b,c reveals the respective element maps for Co and Fe of the same region. The element maps clearly showed that both Co and Fe were located in the same metal NPs. In addition, relatively stronger signals were observed in the Co element map. This result indicated that Co atoms outnumber Fe atoms in these particles as expected. A negligible amount of Si was detected in the NPs. Thus, it can be ruled out that the metal NPs are composed of metal silicides M_xSi_y (M = Co, Fe).

(44) (a) Turgut, Z.; Nuhfer, N. T.; Piehler, H. R.; McHenry, M. E. *J. Appl. Phys.* **1999**, *85*, 4406 (b) Bönnemann, H.; Brijoux, W.; Brinkmann, R.; Matoussevitch, N.; Waldöfner, N.; Palina, N.; Modrow, H. *Inorg. Chim. Acta* **2003**, *350*, 617.

(45) Li, J.; Zeng, H.; Sun, S. H.; Liu, J. P.; Wang, Z. L. *J. Phys. Chem. B* **2004**, *108*, 14005.
(46) Massalski, T. B.; Murray, J. L.; Bennett, L. H.; Baker, H. *Binary Alloy Phase Diagrams*; American Society for Metals: Materials Park, OH, 1986.

Table 3. XPS Determined Elemental Concentrations (Atom %) for the Co−PFS Film Pyrolyzed at 500 °C for 2 h

element	O 1s	Fe 2p	Co 2p	$Co^0/(Co^0 + Co^{2+})$
surface	74.9	10.1	15.0	0
12 nm depth	48.0	24.0	28.0	55
30 nm depth	37.8	26.4	35.8	63
42 nm depth	32.9	27.7	39.4	73

values were perfectly intermediate between the corresponding values of CoO and FeO, which have almost identical crystal structures and lattice parameters (Table 2). This result was consistent with the formation of CoFe alloy NPs on the film surface and their subsequent oxidation by O_2 in air to form Co(Fe)O. The two additional broad rings labeled as 3* and 7* in Figure 6b could be assigned to the α-CoFe phase. In fact, Figure 6b was a superposition of the diffraction patterns of two phases: the Co(Fe)O phase corresponding to the large particles on the film surface and the α-CoFe phase corresponding to the small particles in the underlying layer of the ceramic films.

Both the α-CoFe and Co(Fe)O phases were also observed in the diffraction patterns of the samples pyrolyzed at 600 and 700 °C. At 800 °C and above, only the α-CoFe phase was detected, which is presumably a result of the phenomenon that large particles are more difficult to appreciably oxidize in comparison to small particles due to their lower fraction of reactive surface atoms. As the diffraction patterns of all the investigated ceramic films only contained α-CoFe or Co(Fe)O phase related signals, the SiC/C matrix was essentially amorphous.

(c) Depth Profiling by XPS. The chemical composition of the NP-containing thin film prepared at 500 °C was quantitatively analyzed by XPS. The thin film was examined by Ar^+ sputtering at the four depths of 0 (surface), 12, 30, and 42 nm. The relevant element concentrations of O, Co, and Fe at each depth are given in Table 3. It is important to note that the use of Al Kα radiation caused overlapping of the Fe $2p_{3/2}$ spectral region with the Co $L_2M_{23}M_{45}$ Auger line. As a consequence, the absolute Fe $2p_{3/2}$ intensity is overestimated.

The Si 2p signal was significantly more pronounced at 42 nm compared to that at 30 nm, which was due to Ar^+ sputtering etching of the Si substrate. This finding was consistent with the sample film thickness of about 39 nm, as observed by cross-sectional SEM (Figure 1, series III at 500 °C). As discussed above, oxidation of the surface NPs can take place during storage and sample processing. This was supported by the XPS findings as the content of O exhibited a maximum at the film surface and decreased with depth (Table 3).

The chemical states of Co in the NP-containing thin film were determined by the Co 2p XPS spectra (Figure 7a). At the film surface, the majority of the Co $2p_{3/2}$ signal occurred at a binding energy of 781.0 eV. This value correlated with the typical binding energy of Co^{2+} in CoO (Co_2O_3 at 779.6 eV and Co^0 at 778.1 eV).[47−50] Thus, the chemical state of

Co on the film surface was Co^{2+}, and the presence of Co^{3+} can be ruled out,[50] which was in good agreement with the results obtained by SAED analysis. XPS spectra for deeper layers showed that a new peak appeared at 778.2 eV, suggesting that Co^0 atoms existed in the ceramic matrix.[47] The intensity of the Co^0 signal increased with film depth and correlated with a decrease of the Co^{2+} signal. This indicated that the ceramic matrix protected the Co atoms from being oxidized. It should be noted that the XPS spectra of Co or Fe in the CoFe alloy do not differ from that of the respective pure metal, because of the same chemical state of the metal atom.

The Fe 2p spectra (Figure 7b) showed a signal for Fe^{2+} at 709.5 eV and for Fe^{3+} at 711.0 eV, which can both be observed on the film surface (FeO at 709.6 eV and Fe_2O_3 at 710.9 eV).[51] The Fe^0 signal at 707.0 eV appeared at a depth of 12 nm, and its intensity continuously increased on moving deeper into the film.[52] These pointed to the fact that Fe atoms were also oxidized at the film surface and were stable as Fe^0 in the ceramic matrix.

3. Magnetic Properties of the Thin Ceramic Films Using the MOKE Studies. The magnetic properties of the pyrolyzed films were characterized by hysteresis loop measurements through longitudinal MOKE studies, and time-domain measurements were made through ultrafast magneto-optical probing.[53]

The MOKE effect is a small change in the polarization state of light reflected from a magnetized film, arising from the interaction of oscillating charge with the magnetization of the material.[54] The static magnetic properties of the pyrolyzed films were characterized by hysteresis loop measurements. These were performed by sweeping an in-plane magnetic field and detecting the change of the in-plane magnetization through the longitudinal MOKE signal which was acquired for a beam angle of incidence of 20°. The dynamic response of the magnetization was also tested. For the dynamic measurement, an ultrafast magnetic field transient was applied perpendicular to the plane of the film,[53] and the magnetization response was monitored with a probe beam at normal incidence (a polar Kerr measurement, sensitive to the out-of-plane magnetization component).

Figure 8 shows the hysteresis loop measurements for samples prepared at the pyrolysis temperatures of 600, 700, 800, and 900 °C.[55,56] No signals could be detected for the

(47) Moulder, J. F.; Stickle, W. F.; Sobol, P. E.; Bomden, K. D.; Chastain, J., Eds. *Handbook of X-Ray Photoelectron Spectroscopy*; Perkin-Elmer: Eden Prairie, MN, 1992.
(48) McIntyre, N. S.; Cook, M. G. *Anal. Chem.* **1975**, *47*, 2208.
(49) Chung, K. S.; Massoth, F. E. *J. Catal.* **1980**, *64*, 320.
(50) Khassin, A. A.; Yurieva, T. M.; Kaichev, V. V.; Bukhtiyarov, V. I.; Budneva, A. A.; Paukshtis, E. A.; Parmon, V. N. *J. Mol. Catal. A: Chem.* **2001**, *175*, 189.
(51) Briggs, D.; Seah, M. P. *Particle Surface Analysis*; John Wiley & Sons: Toronto, 1990; Vol. 1.
(52) The ratio of $Fe^0/(Fe^0 + Fe^{2+} + Fe^{3+})$ cannot be estimated because of the overlapping of the Fe $2p_{3/2}$ spectral region with the Co $L_2M_{23}M_{45}$ Auger line.
(53) Freeman, M. R.; Ruf, R. R.; Gambino, R. J. *IEEE Trans. Magn.* **1991**, *27*, 4840.
(54) Hubert, A.; Schafer, R. *Magnetic Domains: The analysis of magnetic microstructures*; Springer: Berlin, Germany, 1998.
(55) For magnetic properties of bulk CoFe alloys, see: Pfeifer, F.; Radeloff, C. *J. Magn. Magn. Mater.* **1980**, *19*, 190.
(56) For magnetic properties of CoFe alloy nanostructures, see: (a) Turgut, Z.; Huang, M.-Q.; Gallagher, K.; McHenry, M. E.; Majetich, S. A. *J. Appl. Phys.* **1997**, *81*, 4039 (b) Corrias, A.; Casula, M. F.; Falqui, A.; Paschina, G. *Chem. Mater.* **2004**, *16*, 3130 (c) Tang, S. L.; Chen, W.; Lu, M.; Yang, S. G.; Zhang, F. M.; Du, Y. W. *Chem. Phys. Lett.* **2004**, *384*, 1.
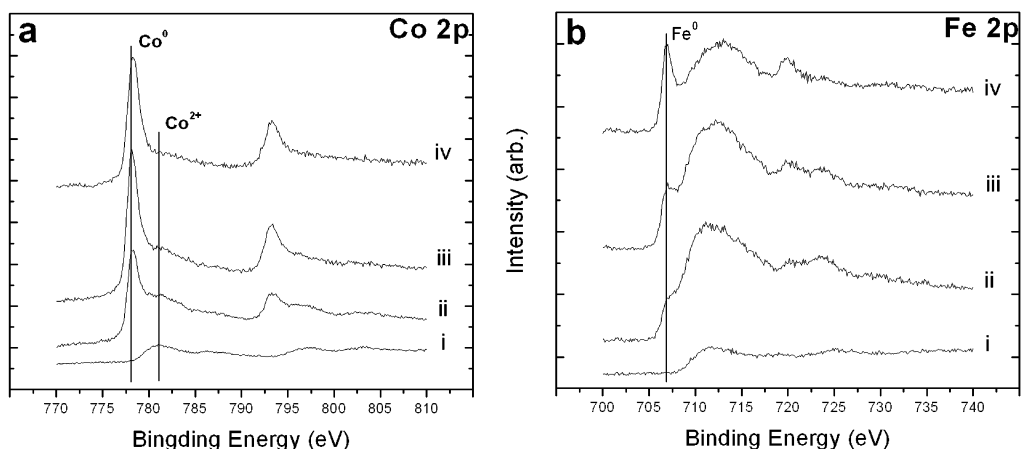
Figure 7. XPS spectra of (a) Co 2p and (b) Fe 2p for Co−PFS (**2**) thin films pyrolyzed at 500 °C for 2 h: (i) surface, (ii) 12 nm, (iii) 30 nm, and (iv) 42 nm depth.
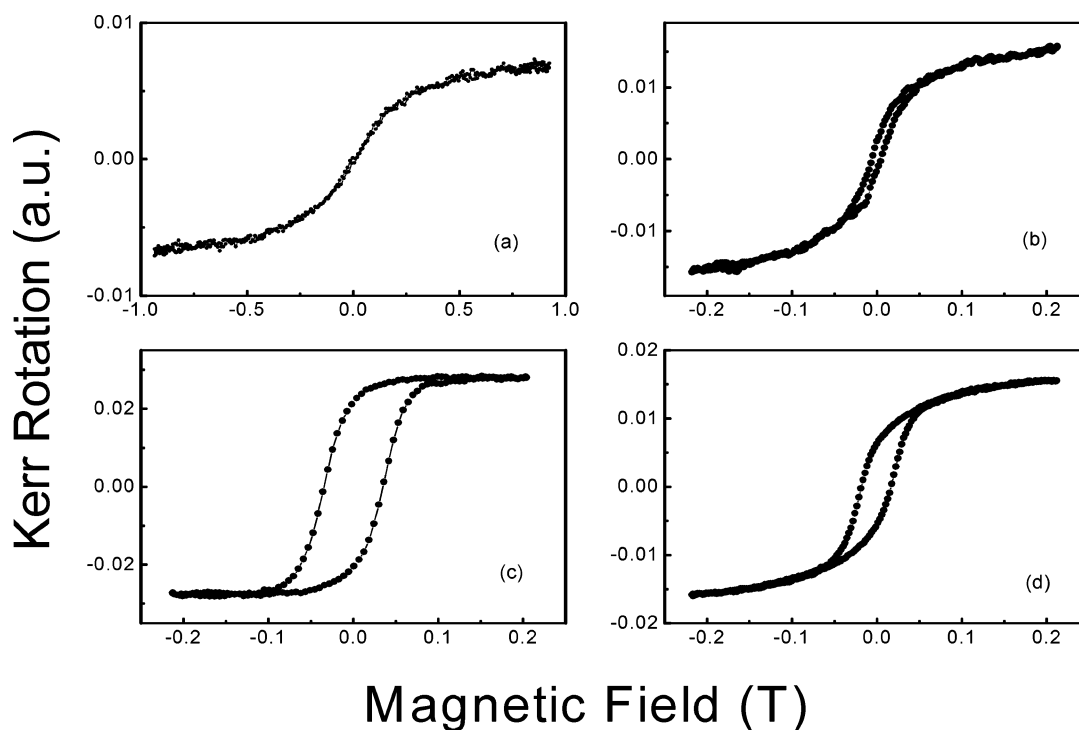

Figure 8. Hysteresis loops of Co−PFS (**2**) thin films pyrolyzed at (a) 600, (b) 700, (c) 800, and (d) 900 °C.

films prepared at 300 and 400 °C, in which NPs were not formed. For the 500 °C sample, surprisingly, a very weak magnetic signal was observed. As discussed above, the film surface was very densely covered with Co(Fe)O NPs. Because both CoO and FeO are antiferromagnetic, it is reasonable to assume that the mixed Co(Fe)O NPs are also antiferromagnetic. The surfaces of these particles may contribute to the weak magnetic behavior, and in addition the dense coverage of Co(Fe)O NPs may obscure the signal from the CoFe NPs in the underlying layer of the film. Figure 8a showed the hysteresis curve of the sample pyrolyzed at 600 °C, which exhibited almost zero remanence and zero coercivity. The magneto-optical response was more than 10 times larger than that of the film formed at 500 °C and must arise from the CoFe NPs. The curve did not reach saturation even at a field strength of 1 T, indicating that the NPs were mainly superparamagnetic. The MOKE investigation on the 700 °C sample yielded a coercivity of 5 mT, with a

magnetization close to saturation at higher field (Figure 8b). In addition, a remanence of approximately 10% of the saturation value was found in the hysteresis loop. At higher pyrolysis temperatures, the size of the individual NP increased; as a result, the NP magnetization became thermally stable on the time scale of this hysteresis measurement, and ferromagnetic behavior was observed. Thus, for the sample formed at 800 °C (Figure 8c) the coercivity further increased to 34 mT and the remanence increased to 74%. In the material prepared at 900 °C (Figure 8d), the particles were large enough to contain a magnetic domain structure, as suggested by the small drop of coercivity to 18 mT and remanence to 65%. Dipolar interactions between single domain particles could also contribute to this tendency. In future investigations we are aiming at further detailed analysis in this respect as the shape and magnetocrystalline anisotropies of the particles critically determine their magnetic behavior in this size regime.
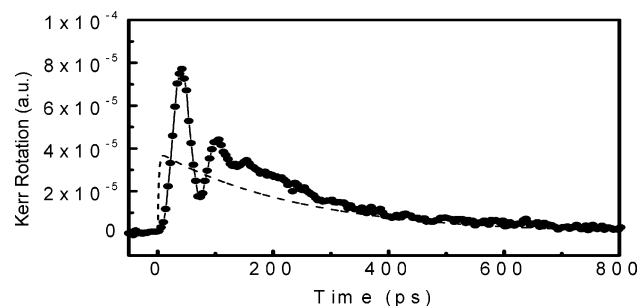
Figure 9. Time-domain MOKE for Co−PFS (**2**) thin films pyrolyzed at 900 °C; the dashed line is a schematic curve of the transient field pulse.

To measure the intrinsic response time of the magnetization in the prepared materials, the sample magnetization was driven from equilibrium by an ultrafast transient magnetic field launched from a femtosecond laser-triggered photoconductive switch in a time-resolved experiment. The transient pulse field resulted in a magnetization change, which was stroboscopically monitored through the MOKE. A femtosecond optical probe beam interrogated the sample with a laser spot size of about 2 μm. The probed area was representative for the ensemble behavior of the entire sample. Figure 9 showed the time-domain curve for the 900 °C sample. In general, the temporal magnetic response follows the shape of the magnetic field pulse, which has a fast rise time but a relatively slow decay, schematically shown in Figure 9 (dashed line). An oscillatory response is superimposed on the pulse shape. These oscillations are ferromagnetic resonances excited by the Fourier components of the broadband excitation pulse that overlap processional frequencies in the sample. However, a sharp resonance as characterized by a long-lived oscillation ring-down was visible. The distribution in particle sizes and the random arrangement of the particles lead to a broad distribution of local effective fields in the sample. The resulting homogeneous broadening of particle resonance frequencies led to high effective damping or complete suppression of temporal oscillation.

In summary, the hysteresis loop measurements show that pyrolysis at higher temperature yielded ferromagnetic CoFe NPs, while superparamagnetic NPs were obtained when the samples were prepared at lower temperature. Time domain MOKE measurements indicated that the particle size distribution and interaction of the NPs led to a broad distribution of precessional frequencies for individual NP magnetizations.

Conclusion

We report the facile fabrication of superparamagnetic and ferromagnetic ceramic thin films containing CoFe alloy NPs in an amorphous SiC/C matrix by means of the pyrolysis of thin films of the highly metallized organometallic polymer Co−PFS (**2**). The pyrolysis temperature strongly affected the composition, structure and properties of the resulting alloy NP-containing materials. At 500 °C smaller NPs are formed in the underlying layer of the ceramic film, while partially embedded uniform larger CoFe NPs formed on the film surface. This is most likely due to the faster diffusion at the two-dimensional phase boundary which facilitates metal atom agglomeration. Pyrolysis of Co−PFS (**2**) at higher temperatures yields larger NPs with a broad size distribution at the film surface.

The CoFe alloy NP-containing thin films prepared at 500 and 600 °C may find applications in spintronic devices as an isolating magnetic layer in a nanogranular in-gap structure.[38] Investigations on the use of these materials for this type of application are in progress and will be addressed in future publications.